J Solid State Electrochem (2012) 16:53–64
DOI 10.1007/s10008-010-1273-8

ORIGINAL PAPER

A study of the charge propagation in nanoparticles of Fe_2O_3 core-cobalt hexacyanoferrate shell by chronoamperometry and electrochemical impedance spectroscopy

Hossein Heli · N. Sattarahmady · S. Majdi

Received: 17 September 2010 / Revised: 2 December 2010 / Accepted: 5 December 2010 / Published online: 24 December 2010

Abstract A composite electrode comprised of graphite, Nujol, and nanoparticles of Fe_2O_3 core–cobalt hexacyanoferrate shell was prepared and the charge transport processes in the bulk of this composite were studied. The electrode/solution interface was assumed as a binary electrolyte whose charge transport occurred between redox sites of the nanoparticles present in the composite and counter cations present in the solution. Using cyclic voltammetry, the diffusion of counter cation in the shell was investigated. Using chronoamperometry, an effective diffusion coefficient and its dependency on the applied potential was obtained. In the Nyquist diagrams, different time constants were appeared with relation to different physical and electrochemical processes. Percolation of electron in the shell of the nanoparticles appeared at very high frequencies and exhibited the feature of a diffusion process with a transmissive boundary condition at interface of core–shell structure/graphite particles. The diffusion coefficients of electron and counter cation and the standard rate constants of each individual electrochemical reaction were obtained.

Keywords Cobalt hexacyanoferrate · Nanoparticle · Core-shell structure · Charge propagation

H. Heli
Laboratory of Analytical and Physical Electrochemistry,
Department of Chemistry, Science and Research Branch,
Islamic Azad University,
Fars, Iran

H. Heli (✉)
Young Researchers Club,
Science and Research Branch, Islamic Azad University,
Fars, Iran
e-mail: hheli7@yahoo.com

N. Sattarahmady
Department of Biochemistry,
Shiraz University of Medical Sciences,
Shiraz, Iran

S. Majdi
Department of Chemistry, K. N. Toosi University of Technology,
Tehran, Iran

Introduction

Nanosized materials have been constantly considered in multidisciplinary researches during past few years due to comparable characteristic length scale with the critical length scales of physical phenomena [1]. This nanosize dimension leads to novel outstanding properties which produce potential applications in electronics, optics, catalysis, electrocatalysis, ceramics, and magnetic data storage [2, 3]. However, size alone is not the defining parameter of many nanosize-derived effects; different shape materials can represent significant different properties. Therefore, much works continue to be undertaken on the synthesis of nanostructured materials with high shape anisotropy [4]. In addition, structure also plays a key role in determining the properties of nanomaterials [3, 5–10]. Depletion of crystal defects, moderation of surface roughness, and expression of crystal faces are additional parameters that contribute significantly to the continuing surge of activity in nanoscience today [11].

Transition metal hexacyanoferrates ($M[Fe(CN)_6]$, MHCFs) are an important class of insoluble mixed-valence polynuclear compounds which have vast applications in electrochromism, potentiometric analysis, electrocatalysis, and sensing devices [12–15]. Nanostructures of MHCFs have been synthesized using protecting or stabi-

lizing polymers [16, 17], template-free precipitation, template-based precipitation, and electrodeposition on indium-tin oxide surface [18]. Nanotubes of carbons have also been employed as nanostructured scaffold to prepare nanowires of MHCFs [18]. Among the MHCFs, cobalt hexacyanoferrate (CoHCF) is an important member which exhibits well-defined and reproducible redox transitions during which it permits transport of alkali metal cations providing charge balance [3, 19–22].

Many studies have been devoted to the understanding charge propagation mechanism in solid ionic matrices [23–25]. A solid ionic material containing redox sites in contact with a liquid electrolyte is a binary electrolyte whose charge transport is occurred between redox sites of the solid material and the charge compensation is performed by the counterions originate from an infinite space of the liquid electrolyte. On the other side, the solid material itself, bears both ionic and electroreactive species. Depending on the experimental conditions (e.g., type of solid matrix, nature and concentration of redox centers, mobility and availability of counterions), the overall charge propagation process can be controlled by a variety of phenomena such as electron self-exchange rate, counterion migration, and ion-pairing [26, 27].

Recently, a lot of interest has been focused on the fabrication of advanced materials consisting of cores covered by shells of different chemical compositions. The morphology and the size of these core–shell materials can be tailored easily by changing the core materials' shape, size, or the shell's thickness. These core–shell nanomaterials represent unique properties which are different from those of single-component materials so they have potential applications in photonic crystals, catalysts, electrocatalysts, diagnostics, and pharmacology [3, 6, 28–30]. We have recently been involved in the synthesis, characterization, and electrochemical applications of CoHCF in a core–shell structure [3, 6, 29, 30]. It has been achieved that the special core–shell structure caused in enhancement the kinetics of redox processes of CoHCF and increment in the electrode reaction kinetics during electrocatalytic reactions when nanoparticles of CoHCF acts as the electron transfer mediator for the electrooxidation of some biologically active compounds. The enhancement in the properties of the core–shell structures has been related to the so-called strain and ligand effects of the core substrate on the shell compound [30, 31].

In the present study, the charge transport process in CoHCF particles with a core-shell nanostructure (n-Fe_2O_3@NaCo[Fe(CN)$_6$]) is investigated.

Experimental

All chemicals used in this work were of analytical grade from Merck and were used without further purification. All solutions were prepared with redistilled water. Nanoparticles of Fe_2O_3 (n-Fe_2O_3) were synthesized via precipitation as described previously [3, 32]. Briefly, 5.0 mL aerated aqueous solution containing 100 mM $FeCl_2$+200 mM Fe$(NO_3)_3$ was added to 50 mL aqueous solution of 2.0 M NaOH under vigorous mechanical stirring for 30 min at 80 °C. The precipitated product was collected and removed from the solution by filtration and was washed with redistilled water. Then, 10 mL solution of 10 mM HCl was added and then washed again with redistilled water until the supernatant solution turned neutral. n-Fe_2O_3 was further used as the "core". It was suspended in 10 mL solution of 100 mM Na_3[Fe(CN)$_6$] containing 10 mM HCl and stirred for about 30 min. Then 10 mL solution of 100 mM $CoCl_3$ containing 10 mM HCl was added, and the resultant mixture was stirred. NaCo[Fe(CN)$_6$] precipitated as the "shell" on the surface of the nucleation centers of n-Fe_2O_3 and produced the core-shell nanostructure. n-Fe_2O_3@NaCo[Fe(CN)$_6$] was then collected, removed from the solution, and washed.

n-Fe_2O_3@NaCo[Fe(CN)$_6$]-based carbon composite electrode (cs-CCE) was prepared by mixing weighed amounts of carbon powder, Nujol and n-Fe_2O_3@NaCo[Fe(CN)$_6$] with a ratio of 70:25:5% *w*/*w* in an agate mortar until a uniform paste was obtained. The composite was packed into a 2 mm diameter cavity at the end of a Teflon tube and the electrical contact was provided with a copper wire. Unmodified carbon composite electrode (u-CCE) was prepared by mixing weighed amounts of carbon powder and Nujol with a ratio of 75:25% *w*/*w*.

Electrochemical measurements were carried out in a conventional three-electrode cell containing 100 mM Na-phosphate buffer solution (PBS) powered by a potentiostat/galvanostat, μ-Autolab, type III, FRA2 (The Netherland). An Ag/AgCl, 3 M KCl and a platinum disk (both from Azar electrode Co., Iran) were used as the reference and counter electrodes, respectively. In impedance measurements, the frequency range of 100 kHz to 50 mHz was employed while the AC voltage amplitude was 10 mV and the equilibrium time was 5 s. The system was run by a PC through FRA and GPES 4.9 software.

Surface morphological studies were carried out using scanning electron microscopy (SEM) on a Tescan Vega II HiVac instrument, equipped with the energy dispersive X-ray elemental analysis (EDX) capability to measure the chemical composition of the nanoparticles. The transmission electron microscopy (TEM) was performed using a CEM 902A ZEISS instrument, with an accelerating voltage of 80 kV. Samples were prepared by placing a drop of the particles-ethanol dispersed solution on a carbon-covered copper grid (400 mesh) and evaporating the solvent.

Results and discussion

SEM and TEM

The structure, chemical composition and redox behavior of n-Fe_2O_3@NaCo[$Fe(CN)_6$] were investigated previously by the methods of IR spectroscopy, X-ray diffraction patterns, X-ray photoelectron spectroscopy, thermogravimetry, and electrochemistry [3]. Surface morphology, size, and structure of n-Fe_2O_3@NaCo[$Fe(CN)_6$] were analyzed by SEM and TEM. Figure 1a and b show SEM micrographs of n-Fe_2O_3@NaCo[$Fe(CN)_6$] with two different magnifications. Near-spherical nanoparticles with an average size of ≈40 nm are observed. Figure 1c shows an EDX spectra of n-Fe_2O_3@NaCo[$Fe(CN)_6$]. Cobalt and iron were detected and it indicates that the nanoparticles comprise both these elements. Figure 1d shows a TEM image of n-Fe_2O_3. Spherical nanoparticles with a mean of 20 nm are witnessed. Figure 1e represents TEM images of n-Fe_2O_3@NaCo[$Fe(CN)_6$] with two different magnifications.

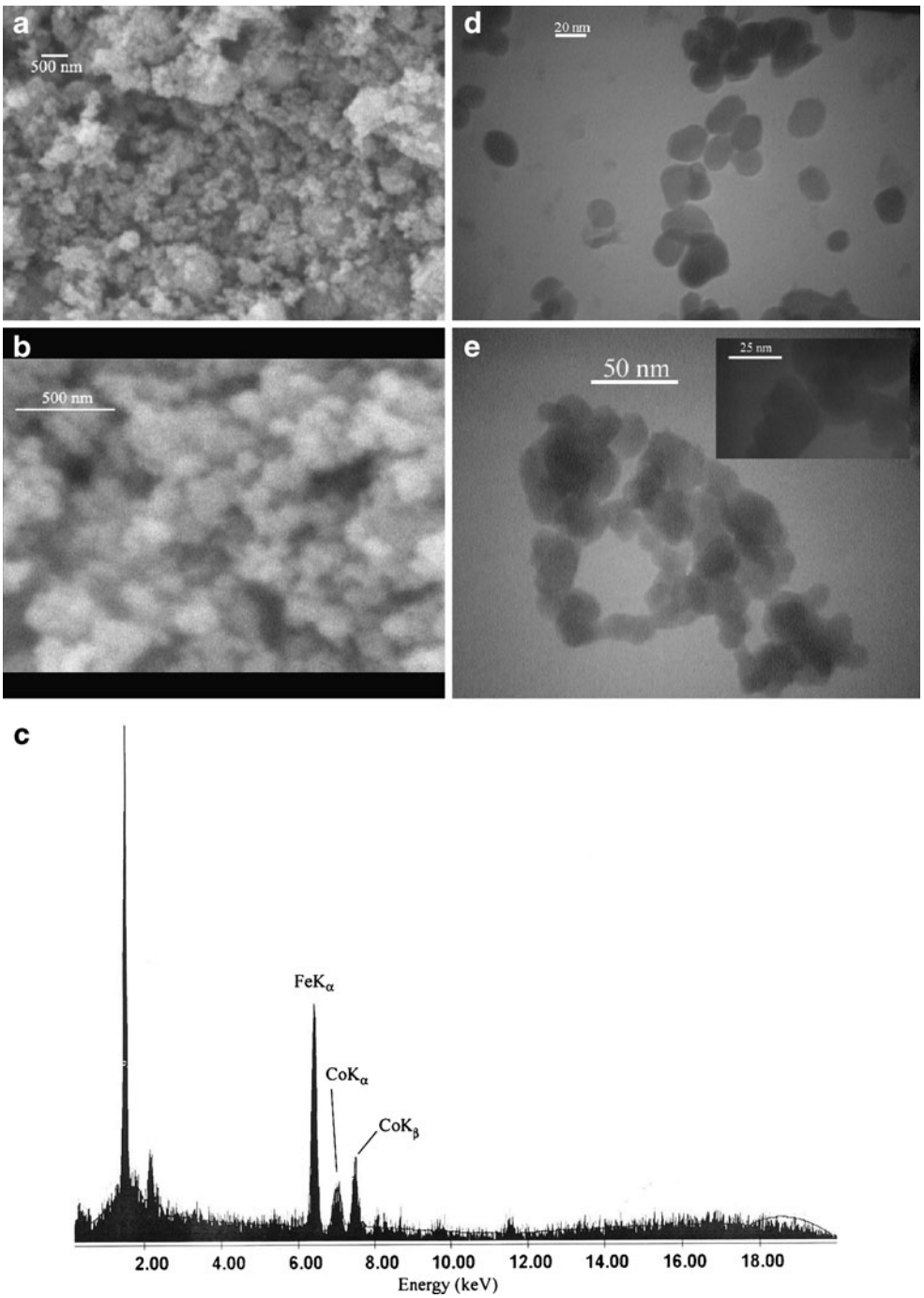

Fig. 1 SEM (**a** and **b**) images, EDX spectra (**c**) and a TEM image of n-Fe_2O_3@NaCo[$Fe(CN)_6$], and a TEM image (**d**) of n-Fe_2O_3

The core–shell structure with shells of 10–30 nm thickness is witnessed.

Chronocoulometry

Multi-step chronocoulometry was performed to determine the number of redox centers of various oxidized and reduced species present in cs-CCE, the active volume and the active surface area. The data are necessary to estimate the diffusion coefficient and the rate of redox reactions. In order to determine the number of oxidized cobalt/iron centers at a certain potential, the electrode was first polarized during 400 s at 0/780 mV to reduce all active centers. Then, the charge for oxidation was measured within the following 400 s at set potentials between 390–490 and 700–900 mV with increment of 10 mV. Similarly, to determine the number of reduced cobalt/iron centers, the electrode was first polarized during 400 s at 780/1,050 mV to oxidize all active centers. Then, the charge for reduction was measured within the following 400 s at set potentials between 490–390 and 900–700 mV with increment of 10 mV. Similar separated measurements were performed using u-CCE in order to subtract the charge of u-CCE from cs-CCPE. From the maximum electric charge, the total numbers of redox centers, n_{tot}, were calculated to be 8.5×10^{-9} and 5.5×10^{-9} mol for cobalt and iron species, respectively.

The total concentrations of cobalt/iron centers in the CoHCF lattice can be calculated using the lattice constant (which is 1 nm [33]) and the number of iron and cobalt centers per unit cell, which is four according to the stoichiometry of the compound (the cubic structure of CoHCF is shown in Scheme 1). Therefore, the total concentration of both cobalt and iron species is $C_{tot}=6.64\times10^{-3}$ mol cm^{-3}.

Based on these results, the active volumes which these active centers were distributed, can be determined using the equation $C_{tot}=n_{tot}/V_{act}$. In this equation, C_{tot} is calculated and n_{tot} is obtained by chronocoulometry measurements. Therefore, the active volumes are obtained as $V_{act}=1.28\times10^{-6}/8.28\times10^{-7}$ cm^3. Accordingly, the active area for the cobalt and iron species, V_{act}, can be obtained using the equation $V_{act}=A_{act}d$, where d is the penetration depth. The penetration depth was taken as equal to the average shell thickness of n-Fe_2O_3@NaCo[$Fe(CN)_6$] (20 nm, vide supra). Hence, it follows that the active areas of cs-CCE are 0.641 and 0.41 cm^2, for cobalt and iron centers, respectively.

Cyclic voltammetry

It has been known that the redox processes of MHCFs involve the transport of charged species (cations) as well as the electron injection within the bulk of these materials (see also Scheme 1) [34, 35]. In the case of cs-CCE/solution interface, these processes occur as: (a) electron transfer at the interface of n-Fe_2O_3@NaCo[$Fe(CN)_6$]/carbon micro-particles, (b) transport of all charged species through the bulk of n-Fe_2O_3@NaCo[$Fe(CN)_6$], (c) insertion/deinsertion of cations across the n-Fe_2O_3@NaCo[$Fe(CN)_6$]/solution interface from/into the bulk of n-Fe_2O_3@NaCo[$Fe(CN)_6$], and (d) ion transport in the bulk of solution. It is taken into account that the charge transport in the bulk of the solution is fast enough not to control the rate of the overall processes because the diffusion coefficient of the cations in the bulk of the aqueous solutions is higher than that in the bulk of MHCFs [13–15].

Figure 2 represents a typical cyclic voltammogram recorded in PBS using cs-CCE at a potential sweep rate of 50 mV s^{-1}. cs-CCE exhibited two well-defined sets of quasi-reversible redox transitions with the corresponding formal potentials of 424 and 845 mV. They are named as transitions I (at lower potentials) and II (at higher potentials), respectively. Transition I is assigned to the redox couple of Co(III)/Co(II) and transition II is related to the redox reaction of Fe(III)/Fe(II) couple in the solid state

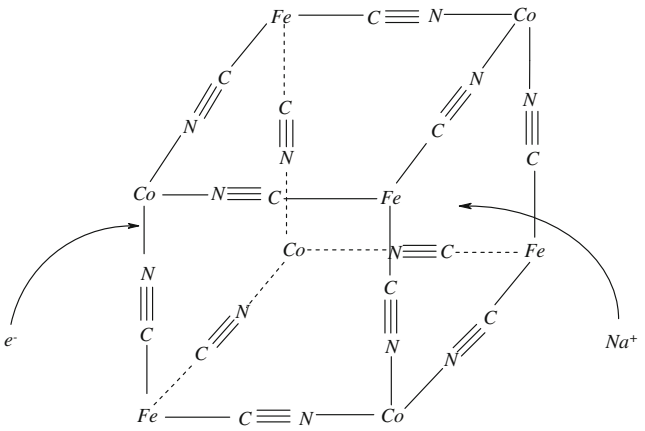

Scheme 1 The cubic structure of CoHCF

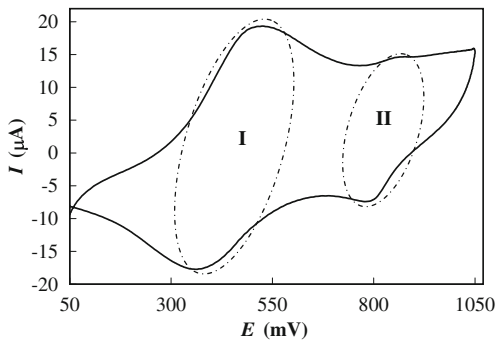

Fig. 2 Typical cyclic voltammogram recorded in PBS using cs-CCE. The potential sweep rate was 50 mV s^{-1}

[19–22]. These redox reactions with the involvement of Na^+ can be expressed as follows [20]:

$$NaCo^{III}\left[Fe^{II}(CN)_6\right] + Na^+ + e^- \rightleftharpoons Na_2Co^{II}Fe^{II}(CN)_6 \quad (1-1)$$

$$Na_{0.4}Co^{III}{}_{1.3}\left[Fe^{II}(CN)6\right] + Na^+ + e^- \rightleftharpoons Na_{1.4}Co^{II}{}_{1.3}\left[Fe^{II}(CN)_6\right] \quad (1-2)$$

$$Co_{1.5}{}^{II}\left[Fe^{III}(CN)_6\right] + Na^+ + e^- \rightleftharpoons NaCo^{II}{}_{1.5}\left[Fe^{II}(CN)_6\right] \quad (2-1)$$

$$Co^{III}\left[Fe^{III}(CN)_6\right] + Na^+ + e^- \rightleftharpoons NaCo^{III}\left[Fe^{II}(CN)_6\right] \quad (2-2)$$

Further analysis of cyclic voltammograms of cs-CCE has been reported recently [3]. Based on those results, a detailed kinetic analysis was performed and it has been concluded that the overall process is solid-state diffusion controlled. This indicated that under the experimental conditions employed for the cyclic voltammetric analysis, the electrode process is propagated only to a certain depth into the n-Fe_2O_3@NaCo[$Fe(CN)_6$]. A standard rate constant is always obtained based on analysis of cyclic voltammograms recorded at different potential sweep rates using Laviron equation [36]. For n-Fe_2O_3@NaCo[$Fe(CN)_6$], two rate constants of 0.38 s^{-1} for transition I and 2.32 s^{-1} for transition II have been obtained [3]. These rate constants are related to the electron transfer processes occurred at the immobilized redox "surface" sites when electrons jump across the electrode/solution interface. On the other hand, cs-MCCE/solution interface can be visualized as a binary electrolyte whose charge transport is occurred between redox sites of the nanoparticles present in the bulk of the composite accompanied by participation of counter cations present in the outermost solution. This leads to the "bulky" electron transfer rate constants. This mater will be taken up in details by impedance spectroscopy (vide infra). It should be noted that cyclic voltammetry does not allow any decision on the entity of the species diffused in the "entire" time scale of the overall process. Diffusion of cations in the bulk of CoHCF is rate limiting in the time scale of cyclic voltammetry when the current approaches the peak. It occurs at the highest time scales (vide infra). On the other hand, the charge propagation during the redox process of n-Fe_2O_3@NaCo[$Fe(CN)_6$] is accompanied by the simultaneous motion of countercation and hopping the electrons to maintain charge balance.

Chronopotentiometry

In chronopotentiometry, the applied current step to a diffusion-controlled system linearly depends on the square root of the transition time according to the Sand equation [37]:

$$I = 0.5nFACD^{0.5}\pi^{0.5}\tau^{-0.5} \quad (3)$$

where A is the electrode area, D is the diffusion coefficient, and τ is the transition time. Figure 3 represents typical double-step chronopotentiograms (with current reversal) recorded in PBS using cs-CCE recorded at different current steps of 1.1–2.2 μA. The potential time curves with well-defined transition times were observed. The ratio of transition times for the direct oxidation and subsequent reduction are 1.5. This indicates that only some parts of redox centers from total redox centers located on cs-CCE participate in the redox processes. The dependency of the product of $I\times\tau$ on $\tau^{-0.5}$ is represented in the inset of Fig. 3. It can be observed that the $I\times\tau$-$\tau^{-0.5}$ relationship does not obey the Sand relation; $I\times\tau$ increases with decreasing transition time and the constancy of $I\times\tau$ with transition time is not observed. Therefore, it can be deduced that the diffusion of the species was potential dependent. This dependency will be deeply investigated by chronoamperometry (vide infra).

Chronoamperometry

Chronoamperometry can characterize the charge transport process in the bulk of n-Fe_2O_3@NaCo[$Fe(CN)_6$]. The

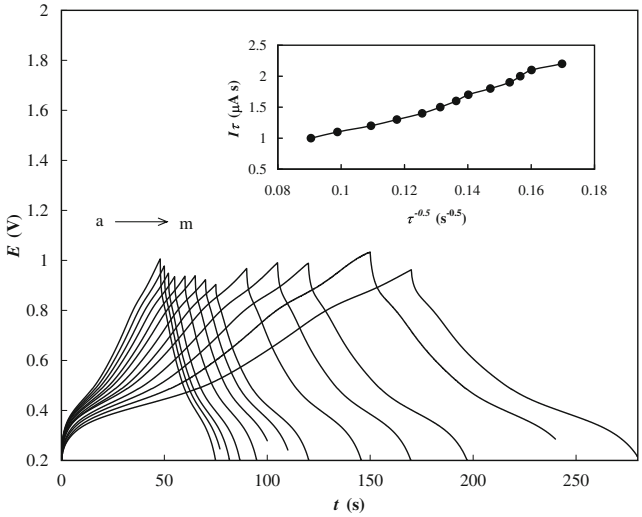

Fig. 3 *Main panel* double-step chronopotentiograms with current reversal recorded in PBS using cs-CCE. The current steps are: 1.1 (**a**), 1.2 (**b**), 1.3 (**c**), 1.4 (**d**), 1.5 (**e**), 1.6 (**f**), 1.7 (**g**), 1.8 (**h**), 1.9 (**i**), 2.0 (**j**), 2.1 (**k**), 2.2 μA (**l**) and 2.3 μA (**m**). *Inset* dependency of $I\times\tau$ on $\tau^{-0.5}$

propagation of charge in the bulk of MHCFs can be interpreted in terms of electron self-exchange reaction and cation transport. The former occurred at a very low time scales and the later dominated at a high time scales. Disregarding controversies about the composition, structure, lattice reconstruction and whether electron or cation diffusion being the rate limiting step of the overall redox process of MHCFs, the overall rate of charge propagation in the MHCFs lattice obeys Fick's low of diffusion. These processes can be inspected in terms of an effective diffusion coefficient (D_{eff}) in the medium time scale. The transient current at a low amplitude potential step in this condition can be expressed as [38]:

$$i(t)/i(0) = \exp\left(\kappa^2 t'\right)\left[1 - \mathrm{erf}\left(\kappa^2 t'\right)^{0.5}\right] \quad (4)$$

where, *i(t)* and *i(0)* are the current densities at a given moment of time and at zero time, respectively, κ is a parameter which is determined by the value of diffusion coefficients of cation, electron, and the ratio between the concentrations of redox sites. Also, $t'=tD_{eff}d^{-2}$ where d is the penetration depth. At the initial stage of diffusion where $0<t<d^2/(\kappa^2 D_{eff})$, Eq. 4 reduces to:

$$i(t) = i(0) - 2i(0)\kappa(tD_{eff}/\pi d^2)^{0.5}\left[1 - \pi(tD_{eff}/d^2)^{0.5}\right] \quad (5)$$

And for the condition that time obeys the inequalities of $(1/\kappa^2)\leq(tD_{eff}/d^2)\leq 1$, Eq. 5 is reduced to:

$$i(t) = (i(0)/\kappa)\left[d^2/(\pi t D_{eff})\right]^{0.5} \quad (6)$$

Equations 5 and 6 indicate that transient current is linearly depended on $t^{0.5}$ or $t^{-0.5}$ in two different time scales. From the linear dependency of the transient current on $t^{0.5}$ and its intercept (Eq. 5), the parameter of $\kappa D_{eff}{}^{0.5}/d$ and $i(0)$ can be obtained. In a parallel manner, the product of the slopes of the linear plots of *i(t)* vs. $t^{0.5}$ (from Eq. 5) and *i(t)* vs. $t^{-0.5}$ (from Eq. 6) is equal to $2i(0)^2/\pi$ which allows to calculate *i(0)*.

Chronoamperograms were recorded for time intervals of 0.1 s in duration of $2\leq t\leq 16$ s in different step potentials. First, the electrode was fixed in an initial potential for 360 s and then was equilibrated for 60 s at the same potential. The potential jumps were adjusted to value of 20 mV. The transient currents generated at different potentials were related to faradaic processes. Time-dependent charging or discharging of double-layer capacitance can be neglected because these processes proceed much faster than diffusion within the electrode. Figure 4 shows the dependencies of *i(t)* on $t^{0.5}$ (A) and $t^{-0.5}$ (B). From the intercepts of the linear plots presented in Fig. 4a, the mean values of D_{eff} for n-Fe_2O_3@NaCo[$Fe(CN)_6$] were obtained at different applied potentials and plotted in Fig. 4c, curve a. Alternatively, from the product of the slopes of the lines represented in Fig. 4a and b, D_{eff} was obtained with respect to the applied potential and represented in Fig. 4c, curve b. Both plots represent similar patterns; D_{eff} changes smoothly and represents two sharp peaks near the formal potentials of redox transitions I and II. Similar behavior for the dependency of D_{eff} on the electrode potential has been reported previously [38, 39]. It should be added that some different values of D_{eff} have been obtained for MHCFs from orders of 10^{-8}–10^{-12} cm^2 s^{-1} by some other authors [40]. The difference between the values of D_{eff} may be a result of the choice of the system and/or supporting electrolyte, measurement approaches, experimental conditions and the assumptions and approximations made about the concentrations of redox sites, homogeneity and thickness of the MHCF materials.

Electrochemical impedance spectroscopy

Electrochemical impedance spectroscopy was also employed to investigate the mechanism of the charge transfer processes in n-Fe_2O_3@NaCo[$Fe(CN)_6$] in a wide range of frequencies. This technique can access relaxation phenomena over many orders of magnitude which yield a

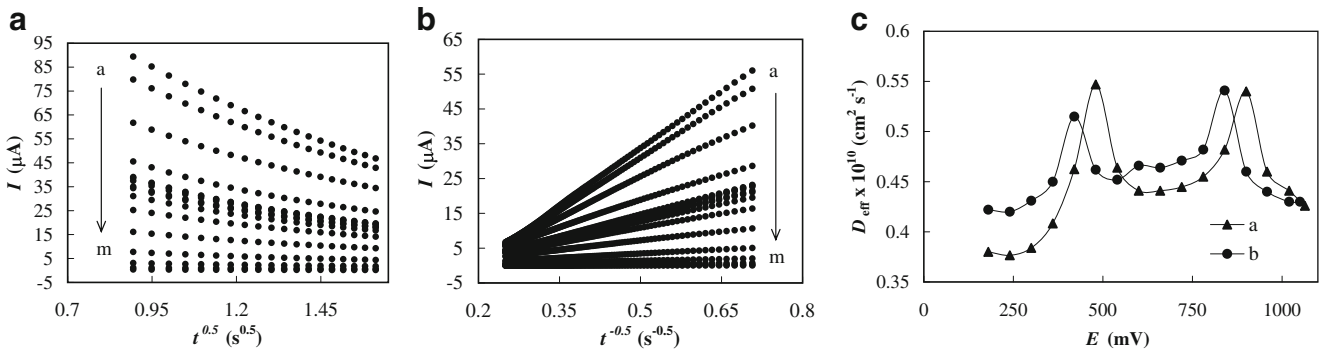

Fig. 4 Dependencies of transient currents, *i(t)*, on $t^{0.5}$ (**a**) and $t^{-0.5}$ (**b**) and D_{eff} on the electrode potential (**c**). The data obtained from chronoamperometric measurements at various potential steps (see text for details)

wealth of data on charge transfer and mass transport processes during redox transitions [7, 24, 41, 42]. As indicated above, physical and electrochemical processes occur in the course of redox reactions of n-Fe_2O_3@NaCo[$Fe(CN)_6$]; these include complex reactions (reactions 1 and 2) involving diffusion of counter cation and percolation of electron within the bulk of the material. Therefore, further clues on the electron transfer and diffusion processes would be witnessed from impedance spectroscopy which may not detectable with other voltammetric techniques employed in this work. The details of these processes are: (1) electron transfer at the interface of electroreactive nanoparticles (n-Fe_2O_3@NaCo[$Fe(CN)_6$])/carbon microparticles (x=0, ions cannot flip/flop at this interface), (2) transport of all charged species (cations and electron) through the bulk of the nanoparticles, (3) diffusion of interstitial cobalt ion in the solid lattice of the nanoparticles, (4) insertion/deinsertion of cations across the nanoparticles/solution interface from/into the solid structure (x=d, d is the shell thickness, electron cannot be injected at this interface), and (5) ion transport in the bulk of solution. Under proper preparation conditions, interstitial cobalt ion can be diminished to a negligible amount. This can be monitored and assured by repeated cyclic voltammetry of CoHCF in the supporting electrolyte [43]. In addition, charge transport in the bulk of the solution did not control the rate of the processes (vide supra).

According to the detailed processes mentioned above, three potential steps can be deduced for cs-CCE in the solution: (1) δE_1: at the interface of n-Fe_2O_3@NaCo[$Fe(CN)_6$]/carbon microparticles, (2) δE_2: through the bulk of n-Fe_2O_3@NaCo[$Fe(CN)_6$] particles, and (3) δE_3: at the n-Fe_2O_3@NaCo[$Fe(CN)_6$] particles/solution interface. Therefore, the faradaic impedance is:

$$Z_{\mathrm{f}} = \delta E_1/\delta I_{\mathrm{f}} + \delta E_2/\delta I_{\mathrm{f}} + \delta E_3/\delta I_{\mathrm{f}} \tag{7}$$

The fluxes of different charged species at two interfaces of n-Fe_2O_3@NaCo[$Fe(CN)_6$]/carbon microparticles and n-Fe_2O_3@NaCo[$Fe(CN)_6$] particles/solution are [39, 40]:

$$\delta J_e/\delta E_1(x=0) = \chi_e/\left\{1+\kappa_e\left[\coth\left[d(j\omega/D_e)^{0.5}\right]/(j\omega D_e)^{0.5}\right]\right\} \tag{8}$$

$$\delta J_C/\delta E_3(x=d) = \chi_C/\left\{1+\kappa_C\left[\coth\left[d(j\omega D_C)^{0.5}\right]/(j\omega D_C)^{0.5}\right]\right\} \tag{9}$$

here

$$\chi_e = \left(C_e - C_{e,\min}\right)\left\{b_e^1 k_e^1 \exp\left[b_e^1\left(E-E_e^0\right)\right]\right\} - C_{e,\mathrm{x}=0}\left(C_{e,\max}-C_{e,\min}\right) \times \left\{b_e^{-1}k_e^{-1}\exp\left[b_e^{-1}\left(E-E_e^0\right)\right]\right\} \tag{10}$$

$$\kappa_e = C_{e,\mathrm{x}=0}\left\{k_e^1\exp\left[b_e^1\left(E-E_e^0\right)\right] - k_e^{-1}\exp\left[b_e^{-1}\left(E-E_e^0\right)\right]\right\} \tag{11}$$

$$\chi_C = b_C^1\, k_C^1\left(C_C - C_{C,\min}\right) - C_{C,\mathrm{soln}}b_C^{-1}k_C^{-1}\left(C_{C,\max}-C_C\right) \tag{12}$$

$$\kappa_C = k_C^1\exp\left[b_C^1\left(E-E_C^0\right)\right] + k_C^{-1}\exp\left[b_C^{-1}\left(E-E_C^0\right)\right]C_{C,\mathrm{soln}} \tag{13}$$

where the subscripts e and C represent electron and cation, respectively. D is the diffusion coefficient of the species through n-Fe_2O_3@NaCo[$Fe(CN)_6$], ω is the angular frequency of the imposed sinusoidal signal, j=$\sqrt{-1}$, $b_e^1 = \alpha nF/RT$ and $b_e^{-1} = (1-\alpha)nF/RT$, C_{e} is the concentration of electrons inserted/deinserted in the shell, $C_{\mathrm{e,max}}$ and $C_{\mathrm{e,min}}$ are the maximum and minimum concentrations available for electron percolation through the shell, respectively, $C_{\mathrm{e,x=0}}$ is a concentration of active sites for electron transfer at the electrode surface, and E_e^0 is a normal potential for the electron transfer reaction. Also, $C_{\mathrm{C,min}}$ $C_{\mathrm{C,max}}$ are minimum and maximum concentration sites available for insertion of cation in n-Fe_2O_3@NaCo[$Fe(CN)_6$], respectively, $C_{\mathrm{C,soln}}$ is the cation concentration in the bulk of solution, and C_{C} is the concentration of occupied sites in n-Fe_2O_3@NaCo[$Fe(CN)_6$]. In these equations, χ is negative for the injection and is positive for the expulsion of cations/electrons.

n-Fe_2O_3@NaCo[$Fe(CN)_6$] is very small-size particles and therefore, δE_2 is negligible in comparison with δE_1 and δE_3. So, the equation of faradaic impedance (Eq. 7) is reduced to:

$$\begin{aligned} Z_{\mathrm{f}} &\approx \delta E_1/\delta I_{\mathrm{f}} + \delta E_3/\delta I_{\mathrm{f}} \\ &= (1/F\chi_e)\left\{1+\left(\kappa_e\tau_e\coth\left(j\omega\tau_e\right)^{0.5}\right)/\left[d(j\omega\tau_e)^{0.5}\right]\right\} \\ &+ (1/F\chi_C)\left\{1+\left(\kappa_C\tau_C\coth\left(j\omega\tau_C\right)^{0.5}\right)/\left[d(j\omega\tau_C)^{0.5}\right]\right\} \end{aligned} \tag{14}$$

where τ_{i}=d^2/D_{i} is the diffusion time constant.

Another approach for the interpretation of impedance response is the model of the wave transmission in a finite-length RC transmission line [41]. This model which was used for a porous electrode or an electroreactive film [44] is:

$$Z_{\mathrm{f}} = R_{ct} + Z_{\mathrm{FLW}} = R_{ct} + R_{\mathrm{FLW}}\left\{g\left(j\omega R_{\mathrm{FLW}}C_{\mathrm{FLW}}\right)^{0.5}/\left(j\omega R_{\mathrm{FLW}}C_{\mathrm{FLW}}\right)^{0.5}\right\} \tag{15}$$

where, R_{ct} is the charge transfer resistance, g is the tangent hyperbolic or cotangent hyperbolic function, R_{FLW} analogizes the resistance of the diffusion of a species through a finite length, and C_{FLW} describes the capacitance of the finite space. In Eq. 15, g is tangent hyperbolic for transmissive

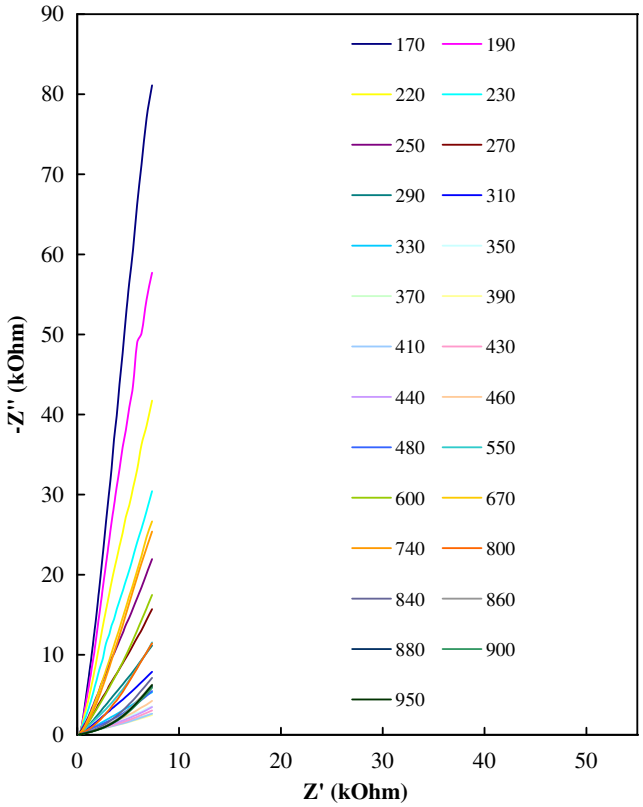

Fig. 5 Nyquist diagrams of cs-CCE in PBS recorded at various dc-offset potentials. The potentials are indicated in mV in the figure

interfaces and is cotangent hyperbolic for reflecting interfaces. Moreover, Z_{FLW} is the impedance of the one-dimensional diffusion of a particle, which is completely analogous to wave transmission in a finite-length RC transmission line. By comparing Eqs. 14 and 15, it can be deduced that:

$$\tau_i = R_{FLW}C_{FLW} = d^2/D_i \tag{16}$$

$$d/\kappa_i\tau_i = R_{ct}/R_{FLW} \tag{17}$$

$$\chi_i = 1/FR_{ct} \tag{18}$$

It should be noted that although the impedance function related to the electron hopping between redox sites and that for diffusion of cation in the bulk of electroreactive material are very similar, the impedance responses related to these processes would be appeared at different frequencies in the Nyquist diagrams. It is due to the differences between the dominated function (tangent hyperbolic or cotangent hyperbolic) and/or the differences between the time constants of the processes. The diffusion of electron and cations in the bulk of MHCFs which occur at the same lengths has very different coefficients (typically, the value of D_e is 10^3–10^8 times higher than D_C [33]). According to Eq. 16, if $D_e >> D_C$, then $\tau_C >> \tau_e$. Therefore, the impedance response of the diffusion of electron should appear at high frequencies, and that for cation should appear at low frequencies.

Figure 5 shows Nyquist diagrams of cs-MCCE in PBS at various dc-potentials of 170–900 mV. In this figure, it is observed that as the bias of the system was systematically varied, different patterns appeared in the diagrams and different processes dominated the electrode reactions. The behavior will be modeled by the dominance of different components in electrical equivalent circuits.

At dc-potential range of 170–230 mV (Fig. 6), a line with a slope ≈1.8 at high frequencies is followed by another linear tail with a slope of near infinity (near vertical line) at low frequencies. This potential range is far from the formal potential of couple I. Therefore, reaction 1 performed with a negligible rate and the charge transfer resistance of this reaction was very large; the corresponding semicircle did not appear in the Nyquist diagrams. The high-frequency line is related to the diffusion of electrons within the bulk of the composite under the applied electric field in a regime of semi-infinite boundary conditions. The low-frequency linear tail is related to the charging of the double layer capacitance. Diffusion of electrons charges the double-layer capacitance and/or performs slow faradaic processes at this potential range. Another point in this figure is that both parts of the impedance curve are deviated from the ideal ones. Semi-infinite diffusion represents a straight line with a slope of unity in the Nyquist diagrams [41]. However, higher slope line appears at high frequencies in the Nyquist diagram. This behavior can be explained in terms of anomalous diffusion [45]: higher slope than unity is observed for semi-infinite diffusion when the diffusing species waits after each jump for a period drown from a broad power–law distribution. The effect is that some diffusing species stick for a long time in diffusion path and diffusion becomes slower. On the other hand, the low-frequency response of the double-layer capacitance is a line

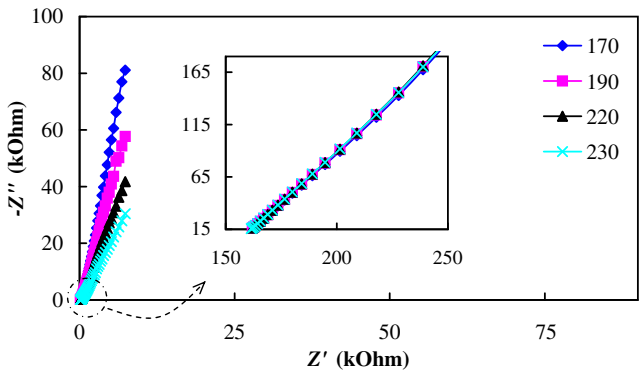

Fig. 6 Nyquist diagrams of cs-CCE in PBS recorded at 170, 190, 220 and 230 mV

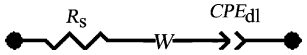

Scheme 2 The electrical equivalent circuit compatible with the Nyquist diagrams represented in Fig. 6

with an infinity slope. However, lower slope line appears at low frequencies in the Nyquist diagrams. This behavior can be characterized using a constant phase element (CPE) instead of the pure capacitance. The roughness at the electrode/interface (local inhomogeneity presents at the electrode surface and non-uniform distribution of local capacities) and consequently, a distribution of activation energies of the processes occurring in the double layer causes the appearance of CPE behavior [43]. The impedance of this element is [46]:

$$Z_{\mathrm{CPE}} = 1/\left[Q_0(\mathrm{j}\omega)^{\mathrm{phi}}\right] \tag{19}$$

where, Q_0 is the constant phase element coefficient and phi is the constant phase element exponent. *phi* is equal to unity for perfect capacitance. The Nyquist diagrams in this dc-potential range can be characterized with the electrical equivalent circuit shown in Scheme 2. In this circuit, R_s, W, and CPE_{dl} are the solution resistance, semi-infinite Warburg element related to the electron diffusion, and a constant phase element related to the double-layer capacitance, respectively.

At dc-potential range of 270–550 mV (Fig. 7) that is around the formal potential of couple I, a depressed semicircle appears at high frequencies. It is followed by two highly depressed semicircles (two arcs) at medium frequencies. At low frequencies, two linear parts appear. In these diagrams, four signatures are observed which they can be better visualized using Bode diagram (typically shown at 424 mV correspond to formal potential of couple I, Fig. 7, inset). In the Bode diagram, the different time constants indicated with vertical arrows. It should be added that the impedance signatures at high frequencies are strongly overlapped and it indicates that the time constants are not very different. At high frequencies, the electron diffusion occurs in a finite length (which is equal to the thickness of n-Fe_2O_3@NaCo[$Fe(CN)_6$]) with a transmissive boundary condition. At very high frequencies, the electrons are not able to reach the spatial boundary and this must leads to a straight line with a 45° slope in the Nyquist diagrams, but it may be not practically observable here. At slightly lower frequencies, the electrons may reach the spatial boundary. When the spatial boundary is an interface with permeability for electrons and therefore it would act as a transmissive interface, one expects that the Nyquist diagram passes from a straight line with 45° slope at high frequencies to a semicircle at slightly lower frequencies. This means that the electron diffusion is followed/preceded by its consumption/generation via performing the redox process of Co(II)/Co(III). Equation 15 was applied for the interpretation of diffusional impedances of electroreactive species in the bulk of thin films [24] or in the Nernst diffusion layer [47], electroinactive ion diffusion in the bulk of a thin film [48], and intercalation process [49]. The Nyquist diagrams in this dc-potential range can be characterized with the electrical equivalent circuit shown in Scheme 3. In this circuit, R_s is the solution resistance, C_e and R_e are, respectively, a capacitance and a resistance related to the electron diffusion in the composite and CPE_{dl} is a constant phase element related to the double layer capacitance. Also, the fine steps of the charge transfer processes (Eqs. 1 and 2) are characterized by the combination of CPE_{dl}-$R_{ct,1}$ and CPE_1-$R_{ct,2}$ and W_o is an open circuit terminus-finite length

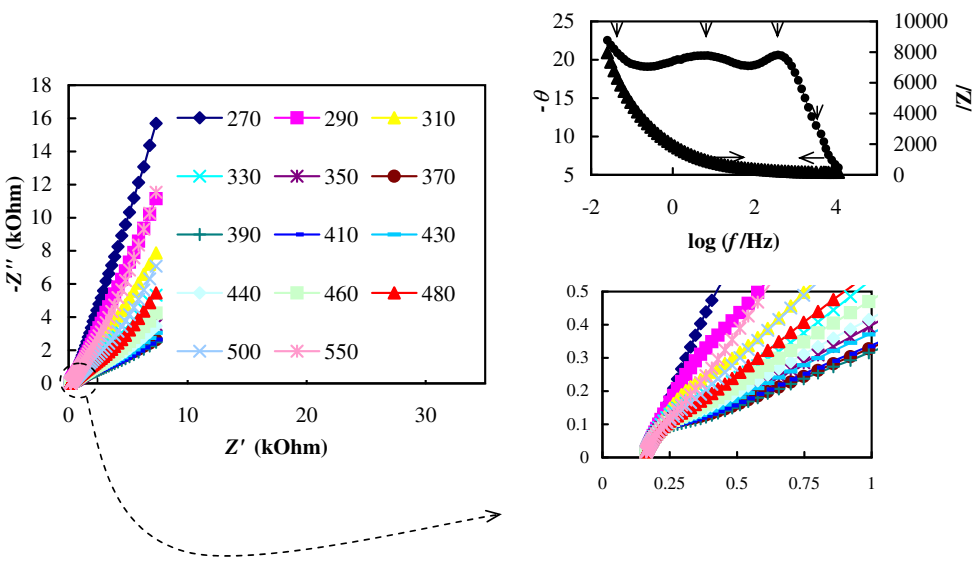

Fig. 7 Nyquist diagrams of cs-CCE in PBS recorded at various dc-offset potentials. The potentials are indicated in mV in the figure. Inset typical Bode diagram recorded at 424 mV

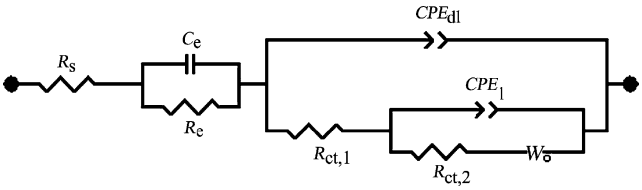

Scheme 3 The electrical equivalent circuit compatible with the Nyquist diagrams represented in Figs. 7 and 8

Warburg element. The values of the electrical element components of this equivalent circuit were obtained by a fitting procedure and reported in Table 1. Using Eq. 15 and the values of R_e and C_e, D_e was obtained as 3.84×10^{-6} cm^2 s^{-1}.

The depressed semicircles which appeared at medium frequencies are related to the couple Co(III)/Co(II) (reaction 2). The electrochemical reactions occurred in couple I involve two different reactions including different chemical species. Therefore, each reaction represents one semicircle in the Nyquist diagrams. It should be noted that it is only impedance spectroscopy that can discerned the fine reactions occurring during this redox couple. From the values of charge transfer resistances obtained from the Nyquist diagram recorded at the formal potential of couple I (see Table 1), the values of exchange currents for the redox processes can be estimated using the equation [37]:

$$R_{ct} = RT/nFi_0 \tag{20}$$

where, i_0 is the exchange current and the other parameters have usual meanings. From the values of the exchange currents, the standard rate constants can be obtained using the equation [37]:

$$i_0 = nFA_{act}k^0 {C_{ox}}^{\alpha} {C_{red}}^{1-\alpha} \tag{21}$$

where, k^0 is standard rate constant, C_{ox} and C_{red} are the concentration of oxidized and reduced centers and α and β are the anodic and cathodic electron transfer coefficients. At the formal potential, C_{ox} and C_{red} are equal and equal to the half of the total concentration of redox species. Two standard rate constants for each redox couples I were so obtained as $k_I^0 = 2.81 \times 10^{-7}$ and 5.70×10^{-8} cm s^{-1}. It should be mentioned that these standard rate constants are related to the charge transport between redox sites of n-Fe_2O_3@NaCo[$Fe(CN)_6$] dispersed in the carbon composite and the counter cations present in the solution as a binary electrolyte.

In the Nyquist diagrams represented in Fig. 7, two linear parts at low frequencies are appeared. Upon increasing the bias from the onset of couple I to the peak potential, the slope of the very low-frequency line decreases from near infinity. Then, it increased again to near infinity. Around the onset potential, the redox reaction is not started and the

Table 1 The values of the equivalent circuit elements obtained by fitting the experimental results in the Nyquist diagrams recorded at two formal potentials of transitions I and II and the corresponding relative errors in percent (represented in parentheses)

Bias/ mV	R_s/Ω	$C_e \times 10^7$/F	R_e/Ω	CPE_{dl}		$R_{ct,1}/\Omega$	CPE_1		$R_{ct,2}/\Omega$	W_o		
				$Q_{0,dl} \times 10^5/\Omega^{-1}$ $s^{phi_{dl}}$	phi_{dl}		$Q_{0,1} \times 10^5/\Omega^{-1}$ s^{phi_1}	phi_1		$R_w \times 10^5/\Omega$	Q_w/s	phi_w
424	150.5 (1.21)	3.35 (2.67)	3.11 (2.26)	3.56 (4.09)	0.64 (3.67)	446.2 (4.74)	9.10 (1.98)	0.32 (1.14)	2,196 (5.01)	86.2 (3.64)	3.05×10^{-3} (6.01)	0.26 (3.24)
845	151.8 (1.25)	3.87 (2.33)	2.68 (2.90)	1.85 (4.17)	0.75 (3.92)	149.5 (4.58)	24.8 (2.62)	0.40 (1.23)	1,796 (5.27)	32.1 (4.18)	77.2 (6.54)	0.40 (3.94)

double layer is still dominated. Around the formal potential, the diffusion–reflection impedance appears. Upon increasing the potential more positive than the formal potential, only the accumulation of cations is dominated and a vertical line is appeared. Cations which are necessary for the charge balance during the redox processes of couple I, are injected to the shell of Fe_2O_3@NaCo[Fe(CN)$_6$]. Then, they reach to a spatial boundary with an interface with no permeability for cation (accumulation of the cation in the bulk of the shell). In addition, it should be mentioned that the anomalous diffusion is again dominated in the system and the impedance signals are deviated from ideal ones. Ideally, the diffusion–accumulation process should represent a line with a slope of unity followed by a line with an infinity slope. However, in the experimental conditions dominated here, the slope of both lines deviated from the ideal ones. It has been reported that deviated linear response which is related to diffusion of ions in the Nyquist diagrams, is observed when the number of diffusing species is not conserved [45] or when the transport of species is driven by drift in the electrical field [50]. Using Eq. 15 with cotangent hyperbolic function, the diffusion of cation (Na^+) in the shell of Fe_2O_3@NaCo[Fe(CN)$_6$] at formal potential of couple I is obtained as 1.31×10^{-9} cm^2 s^{-1}. This value is in agreement with that obtained using cyclic voltammetry elsewhere [3].

At DC potential range of 670–900 mV (Fig. 8) which is around the formal potential of couple II, similar patterns to those appeared in the range of 270–550 mV were observed. In addition, similar equivalent circuit to that of shown in Scheme 3 is employed to characterize the impedance responses. Based on similar discussion, the value of D_e was obtained as 3.86×10^{-6} cm^2 s^{-1} and two values for $k_{II}{}^0$ were obtained as 1.31×10^{-6} and 1.09×10^{-7} cm s^{-1}. Also, D_{Na+} was obtained as 5.18×10^{-14} cm^2 s^{-1}. This value of diffusion coefficient is also in agreement with that obtained using cyclic voltammetry previously [3]. Interestingly, the values of R_e and $T_{0,e}$ are near the same at two formal potentials of couples I and II. Therefore, similar values of D_e are obtained at two potentials. This behavior which has also been reported elsewhere for Prussian Blue [38], is consistent with the band model of conduction mechanism for n-Fe_2O_3@NaCo[Fe(CN)$_6$]. Also, it should be added that two different diffusion coefficients obtained for Na^+ at two formal potentials, may be related to the differences between the stoichiometries and chemical structures of electroreactive species (see reactions 1 and 2).

Conclusion

Nanoparticles of Fe_2O_3 core–cobalt hexacyanoferrate shell were successfully synthesized using a simple precipitation route and were characterized by electron microscopy techniques. They were then incorporated in the bulk of carbon pastes and the mechanism of charge propagation in their complex redox reactions were investigated using different electrochemical techniques. By measuring the charge passed during electrolysis of the electrode, we were able to calculate the effective surface area of the electrode. Then, we developed a model of elementary processes associated with the redox reactions of Co and Fe entities in n-Fe_2O_3@NaCo[Fe(CN)$_6$]. Using cyclic voltammetry, different redox reactions were investigated and it was shown that n-Fe_2O_3@NaCo[Fe(CN)$_6$] represent two redox transitions. The diffusion of cations and electron was measured at different time scales. An effective diffusion, which was affected by both diffusions of cation and electron, dominated at medium time scales and was measured as a function of potential.

A careful interpretation of the impedance data obtained at different DC offset potentials allowed the separation of

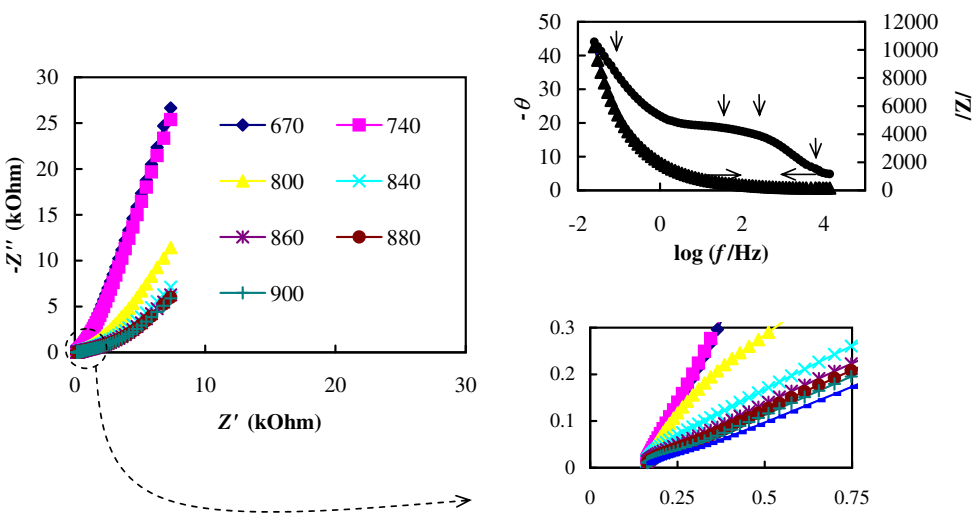

Fig. 8 Nyquist diagrams of cs-CCE in PBS recorded at various dc-offset potentials. The potentials are indicated in mV in the figure. Inset typical Bode diagram recorded at 845 mV

different processes dominated: the diffusion of electron, charge transfer processes with the corresponding fine standard rate constants, and diffusion of counter cation. The electron transport through the nanoparticles toward the reaction zone occurs via a conduction band in graphite particles of the composite, while the electron transport within the reaction zone may be described as electron hopping between the redox centers coupled with the transport of the charge compensating counter cation.

Acknowledgments We would like to thank the Iran National Science Foundation (INSF), the Research Councils of Islamic Azad University, Shiraz University of Medical Sciences, and K. N. Toosi University of Technology for supporting this research.

References

1. Wade TL, Wegrowe JE (2005) Eur Phys J Appl Phys 29:3
2. Nalwa HS (2004) Encyclopedia of nanoscience and nanotechnology. American Scientific Publishers, Los Angeles
3. Heli H, Majdi S, Sattarahmady N (2010) Mater Res Bull 45:850
4. Cao G (2004) Nanostructures and nanomaterials—synthesis properties and applications. Imperial College Press, USA
5. Ebbesen TW, Lezec HJ, Hiura H, Bennett JW, Ghaemi HF, Thio T (1996) Nature 382:54
6. Heli H, Majdi S, Sattarahmady N (2010) Sens Actuators 145B:185
7. Heli H, Hajjizadeh M, Jabbari A, Moosavi-Movahedi AA (2009) Biosens Bioelectron 24:2328
8. Heli H, Hajjizadeh M, Jabbari A, Moosavi-Movahedi AA (2009) Anal Biochem 388:81
9. Sattarahmady N, Heli H, Moosavi-Movahedi AA (2010) Biosens Bioelectron 25:2329
10. Sattarahmady N, Heli H, Faramarzi F (2010) Talanta 82:1126
11. Xiong H, Xia Y (2007) Adv Mater 19:3085
12. de Tacconi RN, Rajeshwar K, Lezna RO (2003) Chem Mater 15:3046
13. Pournaghi-Azar MH, Razmi-Nerbin H (2000) Electroanalysis 12:209
14. Pournaghi-Azar MH, Sabzi R (2002) J Solid State Electrochem 6:553
15. Pournaghi-Azar MH, Razmi-Nerbin H, Hafezi B (2002) Electroanalysis 14:206
16. Uemura T, Ohba M, Kitagawa S (2004) Inorg Chem 43:7339
17. Qu F, Yang M, Lu Y, Shen G, Yu R (2006) Anal Bioanal Chem 386:228
18. Feng LD, Shen JM, Li XH, Zhu JJ (2008) J Phys Chem C 112:7617
19. Lezna RO, Romagnoli R, de Tacconi NR, Rajeshwar K (2002) J Phys Chem B 106:3612
20. de Tacconi NR, Rajeshwar K, Lezna RO (2006) J Electroanal Chem 587:42
21. Tse Y-H, Janda P, Lever ABP (1994) Anal Chem 66:384
22. Kitchin JR, Norskov JK, Barteau MA, Chen JG (2004) Phys Rev Lett 93:156
23. Inzelt G (1994) In: Bard AJ (ed) Electroanalytical chemistry, vol. 18. Dekker, New York
24. Heli H, Yadegari H (2010) Electrochim Acta 55:2139
25. Heli H, Yadegari H, Karimian K (2010) J Exp Nanosci. doi:10.1080/17458080.2010.483694
26. Dalton EF, Surridge NA, Jernigan JC, Wilbourn KO, Facci JS, Murray RW (1990) Chem Phys 141:143
27. Surridge NA, Jernigan JC, Dalton EF, Buck RP, Watanabe M, Zhang H, Pinkerton M, Wooster TT, Longmire ML, Facci JS, Murray RW (1989) Faraday Discuss Chem Soc 88:1
28. Kalele S, Gosavi SW, Urban J, Kulkarni SK (2006) Curr Sci 91:1038
29. Heli H, Majdi S, Sattarahmady N, Parsaei A (2010) J Solid State Electrochem 14:1637
30. Sattarahmady N, Heli H (2010) Anal Biochem 409:74
31. Stamenkovic V, Schmidt TJ, Ross PN, Markovic NM (2003) J Electroanal Chem 554:19
32. Kang YS, Risbud S, Rabolt JF, Stroeve P (1996) Chem Mater 8:2209
33. Kahlert H, Retter U, Lohse H, Siegler K, Scholz F (1998) J Phys Chem B 102:8757
34. Pournaghi-Azar MH, Sabzi R (2003) J Electroanal Chem 543:115
35. Shaoiun D, Fengbin L (1987) J Electroanal Chem 217:49
36. Laviron E (1979) J Electroanal Chem 101:19
37. Bard AJ, Faulkner LR (2001) Electrochemical methods. Wiley, New York, p 310
38. Kondratiev VV, Tikhomirova AV, Malev VV (1999) Electrochim Acta 45:751
39. Garcia-Jareno JJ, Navarro-Laboulais J, Sanmatias A, Vicente F (1998) Electrochim Acta 43:1045
40. Garcia-Jareno JJ, Navarro JJ, Roig AF, Scholl H, Vicente F (1995) Elecirochim Acta 40:1113
41. Barsoukov E, Macdonald JR (2005) Impedance spectroscopy: theory, experiment, and applications, Wiley
42. Gao Z, Bobocka J, Ivaska A (1993) Electrochim Acta 38:379
43. Gao Z, Wang G, Li P, Zhao Z (1991) Electrochim Acta 36:147
44. Pajkossy T (1994) J Electroanal Chem 364:111
45. Bisquert J, Compte A (2001) J Electroanal Chem 499:112
46. Neves RS, Robertis ED, Motheo AJ (2006) Electrochim Acta 51:1215
47. Piela P, Fields R, Zelenay P (2006) J Electrochem Soc 153:A1902
48. Pitarch A, Garcia-Belmonte G, Mora-Sero I, Bisquert J (2004) Phys Chem Chem Phys 6:2983
49. Levi MD, Aurbach D (2005) J Phys Chem B 109:2763
50. Bisquert J, Garcia-Belmonte G, Fabregat-Santiago F, Ferriols NS, Bogdanoff P, Pereira EC (2000) J Phys Chem B 104:2287
51. Gabrielli C, Keddam M, Nadi N, Perrot H (1999) Electrochim Acta 44:2095
52. Gabrielli C, Garcia-Jareno JJ, Keddam M, Perrot H, Vicente F (2002) J Phys Chem B 106:3182